THE JOURNAL OF BIOLOGICAL CHEMISTRY VOL. 286, NO. 27, pp. 23679–23687, July 8, 2011

Water-assisted Proton Transfer in Ferredoxin I*[S]

Received for publication, February 15, 2011, and in revised form, April 29, 2011 Published, JBC Papers in Press, April 29, 2011, DOI 10.1074/jbc.M111.230003

Stephan Lutz, Ivan Tubert-Brohman[1], Yonggang Yang, and Markus Meuwly[2]

From the Department of Chemistry, University of Basel, Klingelbergstrasse 80, 4056 Basel, Switzerland

The role of water molecules in assisting proton transfer (PT) is investigated for the proton-pumping protein ferredoxin I (FdI) from *Azotobacter vinelandii*. It was shown previously that individual water molecules can stabilize between Asp^{15} and the buried $[3Fe\text{-}4S]^0$ cluster and thus can potentially act as a proton relay in transferring H^+ from the protein to the μ_2 sulfur atom. Here, we generalize molecular mechanics with proton transfer to studying proton transfer reactions in the condensed phase. Both umbrella sampling simulations and electronic structure calculations suggest that the PT $Asp^{15}\text{-}COOH + H_2O + [3Fe\text{-}4S]^0 \rightarrow Asp^{15}\text{-}COO^- + H_2O + [3Fe\text{-}4S]^0\,H^+$ is concerted, and no stable intermediate hydronium ion (H_3O^+) is expected. The free energy difference of 11.7 kcal/mol for the forward reaction is in good agreement with the experimental value (13.3 kcal/mol). For the reverse reaction ($Asp^{15}\text{-}COO^- + H_2O + [3Fe\text{-}4S]^0H^+ \rightarrow Asp^{15}\text{-}COOH + H_2O + [3Fe\text{-}4S]^0$), a larger barrier than for the forward reaction is correctly predicted, but it is quantitatively overestimated (23.1 kcal/mol from simulations *versus* 14.1 from experiment). Possible reasons for this discrepancy are discussed. Compared with the water-assisted process ($\Delta E \approx 10$ kcal/mol), water-unassisted proton transfer yields a considerably higher barrier of $\Delta E \approx 35$ kcal/mol.

Water can affect chemical and biological systems at various levels, including the formation of specific interactions through hydrogen bonding, the screening of Coulomb interactions, the mediation of proton transfer, or as an intrinsic component in the secondary structure of proteins. Usually, directly probing this role is difficult because of the transient nature of the processes involved. The difficulty also extends to probing the role of single water molecules in chemical and biological catalysis. Particularly in proton and hydrogen transfer reactions, the role (or absence of it) of water is often postulated but cannot be unequivocally proven. Examples include water involvement in ribozyme catalysis (1) where a large body of data suggests water involvement in RNA backbone trans-esterification or proton transfer in ferredoxin where the experiments were explained as a direct protein-to-[3Fe-4S] cluster transfer without participation of water (2, 3).

There are three profoundly different ways to characterize the role of water in a specific context. First, the water degrees of freedom can be essentially averaged out, and not much insight at the atomistic level can be gained. Second, a few individual water molecules are singled out, and their role can be analyzed in detail. Third, different types of water molecules can be distinguished, for example "surface-bound" *versus* bulk water molecules (4). Individual water molecules have been implicated in mediating proton transfer, and their role has been characterized by spectroscopic means (5). Structural studies, on the other hand, have established that individual water molecules play a central role in protein-ligand interactions such as in carbohydrate-protein binding (6) or in HIV-1 protease (7). In protein folding and protein-protein interactions, water has been found to act as a lubricant or "facilitator" in protein recognition (8, 9), and structural waters can render proteins more flexible (10). Also, it has been argued that water may even be conserved evolutionarily as an integral part of a protein structure (10).

Water has also been suggested to play important roles in proton translocation (11, 12). Two prominent examples are electron transfer processes (13) and ATP hydrolysis (14, 15). In general, proteins performing such proton transfer (PT)[3] reactions are referred to as "proton pumps," among which cytochrome *c* oxidase found in the mitochondrial electron-transfer chain (16–19) and bacteriorhodopsin found in photochemical reaction centers (20–23) are prime examples. Experimental observation of an enzymatic proton transfer has been found by Fourier transform infrared difference spectroscopy (24–26). However, direct experimental observation of PT at an atomistic level is generally difficult because it is a transient process.

Complementary to experimental work, theoretical and computational methods have been used to provide a more detailed understanding of PT processes (27–39). These methods are often based on empirical potentials (29–32), Car-Parrinello, or related approaches (33–37, 39). With standard force fields, it is not possible to examine in detail the dynamics of the proton transfer itself due to their inability to describe breaking and forming of chemical bonds. One way to circumvent this problem is to use mixed quantum mechanics/molecular mechanics calculations (QM/MM) (40, 41). They decompose the system into a part that is directly involved in the reaction and treat it with quantum mechanics, whereas the rest of the system is treated with a molecular mechanics force field. Other methods

* This work was supported by the Schweizerischer National Fonds through Projects 200021-117810 and the National Center of Competence in Research - Molecular Ultrafast Science and Technology (to M. M.).

[S] The on-line version of this article (available at http://www.jbc.org) contains supplemental Tables S1–S3, Figs. S1–S3, additional references, and data.

[1] Supported by a Marie Curie Fellowship (MIF1-CT2006-039088) from the European Commission.

[2] To whom correspondence should be addressed: University of Basel, Klingelbergstrasse 80, 4056 Basel, Switzerland. E-mail: m.meuwly@unibas.ch.

[3] The abbreviations used are: PT, proton transfer; FdI, ferredoxin I; MMPT, molecular mechanics with proton transfer; QM/MM, quantum mechanics/molecular mechanics calculations; MD, molecular dynamics; QM, quantum mechanics; MM, molecular mechanics; PES, potential energy surface; TS, transition state; DFT, density functional theory; UB3LYP, unrestricted Becke 3-parameter (exchange), Lee-Yang-Parr (correlation); PMF, potential of mean force; MEP, minimum energy path.

that use a QM/MM separation are empirical valence bond theory (42) or approximate valence bond theory (43). Recently, we introduced a new method for studying PT in protein-sized systems using molecular dynamics (MD) simulations (44, 45). This approach, named molecular mechanics with proton transfer (MMPT), is inspired by QM/MM simulations but combines a potential energy surface (PES; the "QM" part), suitable for describing the proton transfer between an acceptor and a donor atom, with a force field (the MM part) for the remaining degrees of freedom. The MMPT potential includes a modified treatment of hydrogen bonding that allows for the formation and breaking of bonds involving the proton being transferred (45). The main advantage of this approach over QM/MM is the performance, which is comparable with a force field simulation and makes it applicable for long time simulations of large systems such as proteins. In the present work, we present a generalization of MMPT to condensed phase systems and apply it to proton transfer in ferredoxin (3, 46, 47).

Ferredoxins are a family of small iron-sulfur proteins that mediate electron transfer, which are involved in such fundamental biological roles as photosynthesis and nitrogen fixation (48). One ferredoxin for which considerable amounts of structural and experimental data are available is ferredoxin I (FdI) from *Azotobacter vinelandii*, a nitrogen-fixating soil bacterium. It is known that the one-electron reduction of the iron-sulfur cluster in FdI is immediately followed by the uptake of a proton from the solvent. The mechanism of this proton transfer, which can be used as a model of a redox-driven proton pump, has been the subject of particular attention (46, 3, 49, 50). The kinetics of the electron-coupled proton transfer were probed experimentally using cyclic voltammetry, which, combined with site-directed mutagenesis, indicates that Asp^{15}, a surface residue, plays an important role in catalyzing the proton transfer (51, 3). The simplest possible mechanism would involve a direct (water-unassisted) transfer of the proton from Asp^{15} to give the protonated $[3Fe\text{-}4S]^0H^+$ cluster. However, proton tunneling under such conditions is limited to distances of <0.25 Å (52, 53), and detailed MD and quantum chemical calculations show that the aspartic acid side chain in FdI is too far from the nearest μ_2-sulfur for efficient proton transfer to occur (45, 47). An alternative possibility is that proton transfer between Asp^{15} and S is mediated by a water molecule. Although no crystallographic water molecules near the iron-sulfur cluster were reported, detailed atomistic simulations showed that the active site of FdI is water-accessible and that the active site water is stabilized over extended periods of time and could potentially act as a proton relay (47, 54). It is known from experiment that when interior waters are mobile, they may not be detected in x-ray structures, and in many cases, the number of observed water molecules is smaller than that actually present (55–57). Thus, a water-mediated mechanism is plausible. The overall reaction studied with density functional theory (DFT) and free energy simulations in the present work is Asp^{15}-COOH + H_2O + $[3Fe\text{-}4S]^0 \rightarrow Asp^{15}\text{-}COO^- + H_3O^+ + [3Fe\text{-}4S]^0 \rightarrow Asp^{15}\text{-}COO^- + H_2O + [3Fe\text{-}4S]H^+$. The forward barrier is found to be in good agreement with the experimentally determined rates, whereas the reverse barrier is somewhat overestimated. Contrary to this, the water-uncatalyzed reaction, which is also characterized by density functional theory methods, yields much higher barriers and is unlikely to occur.

MATERIALS AND METHODS

Electronic Structure Calculations—Following the previous study on FdI (54), electronic structure calculations were carried out at the spin-unrestricted level with the UB3LYP DFT functional and a 6–31G(d,p) basis set, using the Gaussian 03 suite of programs (58). Three model systems differing in complexity (models A to C) were considered for scanning the potential energy surface. They are shown in Fig. 1, *A–C*. Model A (33 atoms) includes the $[3Fe\text{-}4S]^0$ cluster (total charge of the system $q = -3$, total spin $S = 2$) with thiomethoxy side chains replacing residues Cys^8, Cys^{16}, and Cys^{49} from FdI; a water molecule coordinating to the S1 atom of the cluster; and acetic acid (AcOH) to model the Asp^{15} side chain from the 7FDR x-ray structure recorded at 1.4 Å resolution (59). Internal bond and angle geometries of $[3Fe\text{-}4S]^0$ initially taken from 7FDR were optimized prior to proton transfer scans in this system. Model B (59 atoms, $q = -3$, total spin $S = 2$) is an extension of model A with a complete representation of residue Asp^{15} and parts (terminated by hydrogen atoms) of residues Cys^{16}, Thr^{14}, and Tyr^{13} to account for interactions of the nearby protein backbone with the proton transfer partners. The geometries of the cluster and amino acid backbone were taken from 7FDR, and the internal coordinates of the Asp^{15} side chain and the water molecule were optimized before the potential energy scans. A version of this model with the water molecule deleted was also used to study water-unassisted proton transfer. For the MMPT parametrization (see below) model system C, including a protonated $[3Fe\text{-}4S]H^+$ cluster with the same thiomethoxy side chains attached as in model A, and a water molecule was used (26 atoms, $q = -2$, total spin $S = 2$; see Fig. 1*C*). Internal bonds and angles of the cluster and all degrees of freedom of the water molecule were optimized prior to calculating the interaction potentials.

Density functional theory scans for the complete proton transfer including the initial transfer (PT1) from Asp^{15}-OH to a water molecule and a second proton transfer (PT2) from the hydronium ion intermediate H_3O^+ to the [3Fe-4S] cluster were performed for models A and B of Fig. 1 along a reaction coordinate defined by the OD1 to HD1 distance $r_{OD1-HD1}$. For both models, internal and external coordinates of water were allowed to relax during the scans, whereas the coordinates of the cluster were kept fixed. This is a reasonable assumption as a comparison of the Fe-S distances between optimized protonated ($[3Fe\text{-}4S]H^+$) and unprotonated ($[3Fe\text{-}4S]^0$) clusters show only small differences (0.05 Å) (59). In model A, all external coordinates of AcOH except the donor oxygen OD1 to proton acceptor atom S1 distance (R_{OD1-S1}) were allowed to relax. R_{OD1-S1} was constrained to three different values: $R_{OD1-S1} =$ 4.4, 4.7 (the value found in the x-ray structure of FdI), and 5.0 Å, resulting in three individual scans for model A. For the energy scan of model system B, only the degrees of freedom of the water molecule and the angle and dihedral connecting HD1 to OD1 of Asp^{15}, were optimized at each point of the scanning coordinate. Relaxing more degrees of freedom is computationally very demanding for this structure. Each scan in model sys-

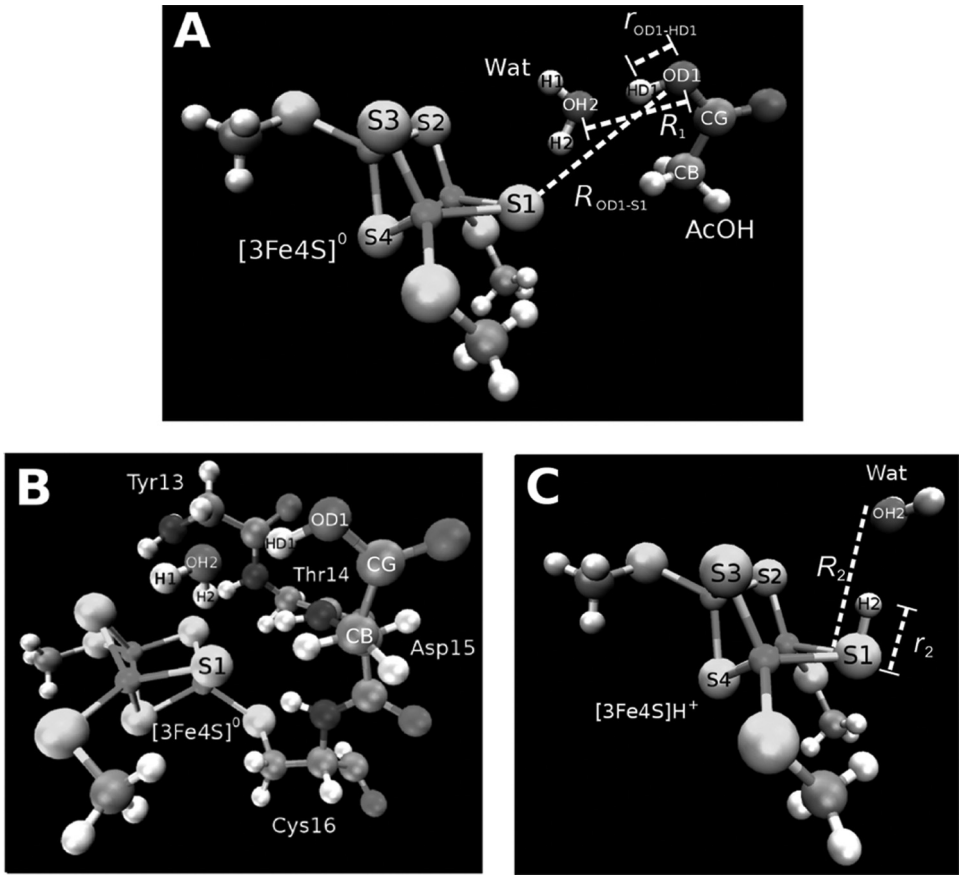

FIGURE 1. *A*, small model system used in the DFT energy scan. *B*, large model system for the DFT energy scan. *C*, model system used to calculate the two-dimensional PES used for fitting MMPT function. *Wat*, water.

tems A and B in Fig. 1 was performed along $r_{OD1-HD1}$. Starting from $r_{OD1-HD1} = 0.8$ Å, the distance was increased in steps of 0.1 Å until the transition state (TS) was reached, and atom H2 of the water molecule was transferred to S1 of the [3Fe-4S] cluster. Close to the transition state, the step size was reduced to improve the resolution of the potential scan in this region.

To parametrize the MMPT potential for PT2 $H_3O^+ + [3Fe\text{-}4S]^0 \rightarrow H_2O + [3Fe\text{-}4S]H^+$, a two-dimensional scan of the potential energy surface was calculated starting from the energy-optimized model C in Fig. 1*C*. The S1 to OH2 distance R_2 and the S1 to HS distance r_2 along the hydrogen bond were scanned, whereas all other degrees of freedom were kept rigid. A total of 347 points were calculated. The resulting energy surface (shown in Fig. 2*A*) has a single minimum that corresponds to having the proton closer to S1, forming a strong hydrogen bond to the water molecule (see Fig. 1*C*).

MD Simulations and Intermolecular Interactions—All atomistic simulations were carried out with CHARMM (60) and the CHARMM22 force field (61) with provisions for the MMPT potential (45). Further details of the simulations are given below and in the supplemental data. Conventional force fields cannot describe the breaking or formation of bonds because stretching potentials are typically parametrized as harmonic oscillators. In contrast, MMPT uses a functional form for $V_{PT}(R, \rho, \theta)$, which is based on Morse potentials and allows for describing proton or hydrogen transfer between D and A. The total potential energy of the system with respect to all coordinates $\vec{x}$ is decomposed into a part for the proton transfer motif ($V_{PT}(R, \rho, \theta)$) and the remaining degrees of freedom $\vec{y}$ of the system. Thus, the total interaction is written as shown in Equation 1,

$$V(\vec{x}) = V_{PT}(R,\rho,\theta) + V_{MM}(\vec{y}) \quad \text{(Eq. 1)}$$

where R is the distance between the heavy atoms, ρ is the PT progression coordinate, defined as $\rho = (r - 0.8)/(R - 1.6)$, and θ is the hydrogen bonding angle. In the following, PT1 takes place between Asp[15]-COOH and water (OD1-HD1···OH2) and PT2 between [3Fe-4S] and water (S1-H2···OH2) (see Fig. 1). According to this definition, PT1 and PT2 start at each end of the overall PT reaction and develop toward the hydronium ion. Thus, for PT1, θ is the hydrogen bonding angle, OH2-HD1-OD1, and for PT2, it is OH2-H2-S1. Subsequently, the variables R_1, ρ_1, and θ_1 refer to PT1 and variables R_2, ρ_2, and θ_2 to PT2.

A consequence of using a large model system such as the one in Fig. 1*C* as a reference for fitting is that nonbonded interactions beyond the immediate vicinity of the proton transfer play a potentially important role. This is unlike the case of the prototype systems used previously, such as $H_5O_2^+$, where these interactions are included in V_{PT2} (62). As a result, it is no longer appropriate to fit V_{PT} directly to the DFT potential energy surface because that would result in double counting of the nonbonded interactions when V_{PT} is added to the CHARMM force field. Instead, V_{PT} has to be fitted to the difference between the DFT energy, and the energy computed using the force field

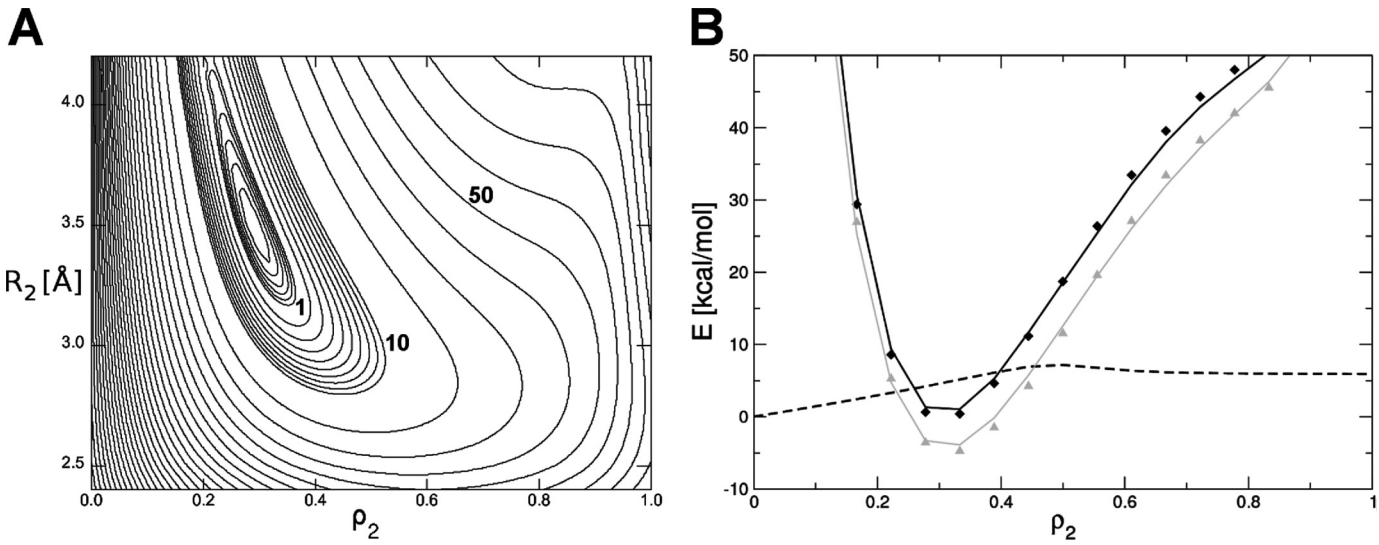

FIGURE 2. *A*, contour plot of the potential energy surface resulting from the DFT scan on model C along $\rho_2 = (r_2 - 0.8)/(R_2 - 1.6)$ and R_2. *B*, example of the fitting process used to avoid double counting of the molecular mechanics nonbonded terms. V_{PT} is fitted to the difference between the DFT energy and V_{MM}. The slice shown is for constant $R_2 = 3.36$ Å. *Black diamonds*, $V^{ref}(\vec{x})$, which is DFT energy; *dotted black line*, $V_{MM}(\vec{y})$, which is the MM energy calculated when V_{PT} is set to 0; *gray triangles*, $V^{ref}(\vec{x}) - V_{MM}(\vec{y})$; *gray line*, $V_{PT}(R_2, \rho_2, \theta_2)$, obtained from a least-squares fit of the asymmetric double minimum potential shown in the supplemental data to the *gray triangles*; *black line*, total fitted MMPT potential $V^{fit}(\vec{x})$.

when V_{PT} is set to zero (from Equation 1, $V_{PT}(R_2, \rho_2, \theta_2) = V(\vec{x}) - V_{MM}(\vec{y})$. This relation is shown graphically in Fig. 2*B* for PT2. The difference between the potential including double-counted interactions (V_{PT2}, *black curve* in Fig. 2*B*) and that without it (*gray curve* in Fig. 2*B*) remains nearly constant in the region where PT takes place. V_{PT2} is shifted by ≈ 6 kcal/mol after subtraction of $V_{MM}(\vec{y})$. For the problem studied here, this means that total energies are moderately influenced by double counting, whereas the PT barrier remains nearly unaffected. The procedure of refitting the surface to account for the double counting of nonbonded interactions is described in detail in the supplemental data.

To distinguish between the different protonation states, the following nomenclature is used: "state 1" has Asp^{15} protonated (-COOH), "state 2" has the water molecule protonated (H_3O^+), and "state 3" has the iron-sulfur cluster protonated ([3Fe-4S]H^+). As a first approximation, the transition between state 1 and state 2, and between state 2 and state 3 may be assumed to lie at $\rho_1 = \rho_2 \approx 0.5$. However, this assumption can be refined based on the shape of the free energy surface obtained from the simulations.

Potentials of Mean Force—One-dimensional potentials of mean force were calculated from MD simulations using umbrella sampling (63). The simulations were started from an equilibrated structure of the reduced protein (Protein Data Bank code 7FDR) at 300 K in a 62 Å cubic TIP3P (64) water box with periodic boundary conditions. The time step in the simulations was 0.5 fs, and all bonds to hydrogen atoms except for those in the water molecule involved in the proton transfer were constrained using the SHAKE algorithm (65). The potentials of mean force are built from individual 50-ps simulations (after 2 ps of further equilibration) with harmonic biasing potentials ranging from $k_{umb} = 30$ to 600 kcal mol^{-1} along the reaction coordinates. To follow PT1, the driving coordinate was defined as $\lambda_1 = r_1/R_1$, where r_1 is the OD1-HD1 distance, and R_1 is the OD1-OH2 distance (see Fig. 1*A*). The corresponding coordinate for PT2 is $\lambda_2 = r_2/R_2$, where r_2 is the S1-H2 distance, and R_2 is the S1-OH2 distance already used above. λ_1 and λ_2 were modified in intervals of 0.05 along the umbrella sampling simulation. The λ-coordinate was chosen as a proxy for ρ for practical reasons. A graphical representation for the relationship between ρ and λ is given in the supplemental data. To account for some of the charge transfer that accompanies proton transfer, atomic charges appropriate for each value of the reaction coordinates were modified (see supplemental data). The data from individual simulations was combined with a weighted histogram analysis (66).

Minimum Energy Pathway—The potential energies along λ_1 and λ_2 were also calculated starting from the MMPT-equilibrated protein structures in states 1 and 3, respectively, with both proton transfers occurring toward state 2. The absolute minimum along the PT scan was determined prior to constraining the system at different values of λ by running 1000 steps of steepest-descent minimization followed by multiple steps of adopted basis Newton-Raphson minimization with a gradient-based cut-off of 10^{-6}. Subsequent adopted basis Newton-Raphson minimization with the same average gradient tolerance were carried out starting from the minimum energy structures by constraining the system to the average λ-geometries obtained from each individual umbrella sampling window.

RESULTS

Proton Transfer from DFT Calculations on Model Systems—Potential energy scans as described in "Materials and Methods" were carried out for model systems A and B (Fig. 1, *A* and *B*) along the OD1-HD1 distance r_1. This yields the minimum energy path (MEP) for double proton transfer and allows to identify the geometries of formation and decomposition of the intermediate H_3O^+ species. Furthermore, it is possible to locate the transition state. The corresponding MEPs are shown in Fig. 3. The initial transfer (PT1) from acetate to the water molecule, which leads to $AcO^-\cdots H_3O^+$, completes at $r_1 = 1.40$

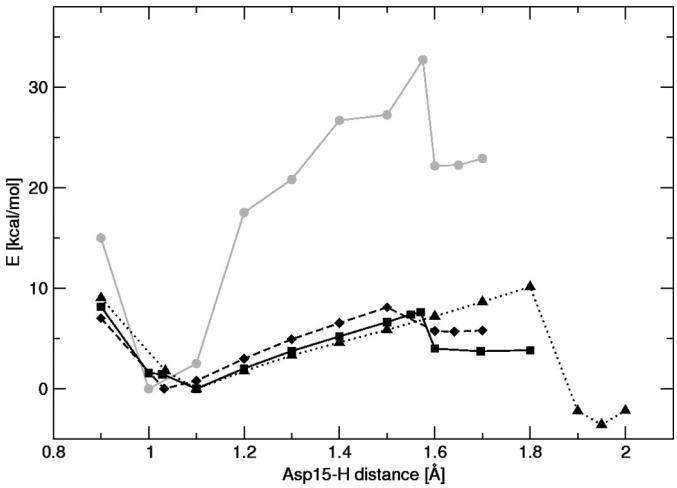

FIGURE 3. **Coupled PT MEPs calculated by DFT for model systems A (*black*) and B (*gray*) as described under "Materials and Methods."** Scans of model system A were calculated for fixed OD1 to S1 distances of 4.4 Å (*solid line*), 4.7 Å (*dashed line*), and 5.0 Å (*dotted line*).

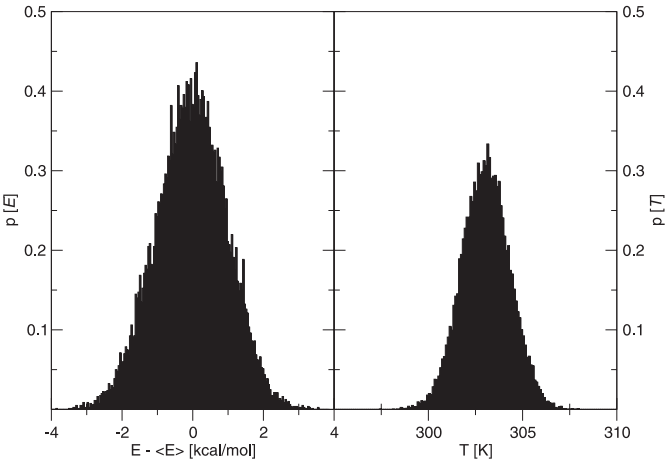

FIGURE 4. **Validation for energy conservation in an MMPT MD simulation of FdI.** *Left*, histogram of the energy fluctuations around the mean from a 100-ps simulation. *Right*, fluctuation of the temperature from the same simulation.

Å, R_1 = 2.50 Å, and ρ_1 = 0.66 in all four scans. None of the potentials show a local minimum at this point, *i.e.* H_3O^+ is energetically not stabilized. Rather, the energy continuously increases along the progression coordinate until the second transfer (PT2) from H_3O^+ to $[3Fe\text{-}4S]^0$ takes place. Therefore, the overall proton transfer from AcOH (or Asp) to $[3Fe\text{-}4S]^0$ involves only a single TS. The initial transition to H_3O^+ (PT1) in model A, located at $r_1 \approx 1.4$ Å, has relative energies of 5.2, 6.5, and 4.7 kcal/mol for R_{OD1-S1} = 4.4, 4.7, and 5.0 Å, respectively. The TS barrier for double proton transfer is located at r_1 = 1.57, 1.50, and 1.80 Å with energies of 7.6, 8.1, and 10.1 kcal/mol for R_{OD1-S1} = 4.4, 4.7, and 5.0 Å, respectively. For R_{OD1-S1} = 4.4 and the larger 6–311G(d,p) basis set, this increases from 7.6 kcal/mol to 10.0 kcal/mol.

For model B, only one scan was carried out for R_{OD1-S1} = 4.8 Å. The TS for the forward double-PT reaction is at r_1 = 1.58 Å with a barrier of 30.2 kcal/mol. The difference between models A and B is related to the fewer degrees of freedom that are allowed to relax in model B. Thus, the system has more strain, which is also indicated by the much steeper slope of the surface. On the other hand, the back transfer barrier of this model system is only 8.1 kcal/mol. Overall, the electronic structure calculations consistently find no stabilized intermediate (H_3O^+), and the barrier for proton transfer is sensitive to rearrangements in the Asp^{15} side chain, which are possible only for the relaxed model A scans.

It is also possible that such a concerted PT reaction involves electronic coupling. To test this, a reverse scan was performed for R_{OD1-S1} = 4.4 Å starting in state 3. The energy of the transition state differs by only 0.2 kcal/mol compared with the forward scan but because the potential energy surface is flat around the transition state, the S1-H2 distance differs by ≈ 0.25 Å between the two structures. Despite this considerable geometrical difference the largest deviation between the Mulliken charges of the atoms involved in PT does not exceed 0.07 *e*. Thus, the different states are not coupled electronically, and the process is ground-state proton transfer.

Reactions PT1 and PT2 from Umbrella Sampling—To validate the MMPT force field in the protein environment, constant energy MD simulations were carried out. For this, 100 ps were run starting from an equilibrated structure of solvated 7FDR. All hydrogen atoms, except for the hydrogen atoms in the water molecule as well as the proton being transferred, were constrained using SHAKE (65). A time step of 0.5 fs was used to follow the rapid H-motion explicitly. Fig. 4 reports the histogram of $E_{tot}(t)$ and temperature $T(t)$, which show no drift over the time interval studied here and establish that the computational procedure is reliable and meaningful.

The experimental rate constant describing proton transfer from the protein (Asp^{15}) to the $[3Fe\text{-}4S]^0$ cluster was determined from fast scan protein film voltammetry at pH 8.34 as $k_{on}^{hop} = 1294 \pm 100\ s^{-1}$ and the back transfer rate from $[3Fe\text{-}4S]^0H^+$ to the protein (Asp^{15-}) as $k_{off}^{hop} = 332 \pm 25\ s^{-1}$ (2). According to transition state theory, such a rate k^{TST} is related to the free energy of activation $\Delta G^{\ddagger}$ by Equation 2,

$$k^{TST} = \left(\frac{k_B T}{h}\right) e^{-\Delta G^{\ddagger}/RT} \qquad \text{(Eq. 2)}$$

where k_B is the Boltzmann constant, T is the temperature in K, h is the Planck's constant, and R is the gas constant (67). From the experimental rate constants (k_{on}^{hop} and k_{off}^{hop}) free energies of activation $\Delta G_{on}^{\ddagger}$ = 13.3 ± 0.05 and $\Delta G_{off}^{\ddagger}$ = 14.1 ± 0.05 kcal/mol for the forward and backward reaction are obtained, respectively. Such barriers are too large to be accessible to unconstrained molecular dynamics simulations. Therefore, the reactive steps were in the following investigated by using umbrella sampling (63).

The first proton transfer (PT1) Asp^{15}-COOH + $H_2O \rightarrow Asp^{15}$-$COO^-$ + H_3O^+ was reinvestigated with the asymmetric potential energy surface (see Ref. 45) but now included fluctuating charges on the atoms involved in the proton transfer motif (see "Materials and Methods" and supplemental Fig. S3). The potential of mean force from umbrella sampling simulations is shown in Fig. 5*A* (*solid line*). The free energy curve does not show a barrier but a characteristic flattening around λ_1 = 0.56,

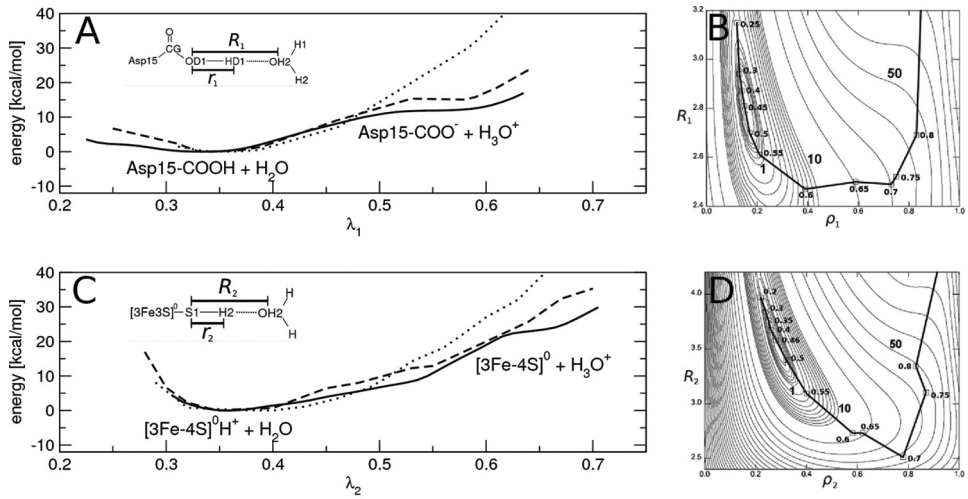

FIGURE 5. Shown are gas phase MEP (*dotted line*), condensed phase MEP from MMPT minimizations in protein (*dashed line*), and PMF from MMPT MD simulations in protein (*solid line*) described for PT1 (*A*) and PT2 (*C*) along $\lambda_1 = r_1/R_1$ and $\lambda_2 = r_2/R_2$, respectively. r_1, R_1, r_2, and R_2 are described in the *insets* of *A* and *C*. *B* and *D*, average trajectories followed during the PMF simulations on the $\rho_1 = (r_1 - 0.8)/(R_1 - 1.6)$, R_1 surface for PT1 (*B*) and on the $\rho_2 = (r_2 - 0.8)/(R_2 - 1.6)$, R_2 surface for PT2. The contour plot show the DFT PES. The *squares* represent average coordinates from each MD simulation, labeled according to the center of the umbrella potentials.

which is related to formation of H_3O^+. This configuration is $\Delta G^{\ddagger}_{PT1} = 11.7$ kcal/mol above the Asp^{15}-COOH + H_2O state, which is somewhat higher than in the earlier work, which was 8.2 kcal/mol (45). This difference is related to the use of fluctuating charges in the present work, which takes into account partial charge transfer from OD1 of Asp^{15} to OH2 of water (for PT1) and subsequently to S1 of the cluster (for PT2), see supplemental data. The *dotted* and *dashed curves* in Fig. 5*A* correspond to the gas-phase minimum energy path from PES 1 and the path calculated in the condensed phase (protein) environment. The gas-phase minimum is shifted from $\lambda_1 = 0.34$ to $\lambda_1 = 0.36$ compared with the minimum energy path (from condensed phase minimizations) and the potential of mean force (from MD simulations), respectively. Fig. 5*B* reports a projection of the average PT coordinate from umbrella sampling onto the corresponding potential energy surface from DFT calculations from Ref. 45. In the minimum of state 1, R_1 lies between 2.8 to 2.9 Å. Decreasing λ_1 increases R_1 and thus separates the water from Asp^{15}. As the reaction progresses, the water approaches $R_1 = 2.5$ Å, and as soon as the proton is completely transferred (in state 2; $\rho_1 \approx 0.7$), R_1 rises again with increasing λ_1, which corresponds to the positively charged hydronium ion moving away from the deprotonated Asp^{15} residue.

For PT2, the potential of mean force is shown in Fig. 5*C* as a *solid line*. The minimum at $\lambda_2 = 0.36$ corresponds to the proton closer to the S1 sulfur atom (although forming a strong hydrogen bond with the water molecule). For comparison, the gas-phase minimum energy path from the potential energy surface in Fig. 2*A* is also shown (*dotted line* in Fig. 5*C*). The two curves are qualitatively similar, although the MEP rises more steeply at higher λ_2. The *dashed line* represents the condensed phase minimum energy path. Between $\lambda_2 = 0.4$ and 0.5, the curve is ≈ 3 kcal/mol higher than the gas-phase MEP but for $\lambda_2 > 0.5$, it lies between the gas-phase MEP and the condensed phase PMF. This suggests that the protein environment provides additional stabilization of the hydronium ion. State 2 appears around $\lambda_2 = 0.65$ in Fig. 5*C*, where the gradient of the potential of mean force flattens out. The corresponding free energy difference relative to H_2O + [3Fe-4S]$^0H^+$ is $\Delta G^{\ddagger}_{PT2} = 23.1$ kcal/mol. Fig. 5*D* shows the average trajectory of the PMF projected onto the R_2, ρ_2 surface. At small ρ_2, the water molecule is far from the S1 sulfur ($R_2 = 4.0$ Å). The initial increase of ρ_2 is primarily related to a reduction of R_2, *i.e.* the water molecule shifts toward the acceptor S1. The actual PT2 takes place at $R_2 \approx 2.5$ Å. Beyond $\rho_2 = 0.8$, R_2 increases again, which corresponds to the completed formation of the hydronium ion. Subsequently, it is detached from the [3Fe-4S] cluster without the formation of a stable minimum. Thus, the overall proton transfer reaction is most likely concerted.

Having identified proton transfers PT1 and PT2 separately with both exhibiting a flattening of the PMF around state 2, it is also possible to connect the two processes. This amounts to a diabatic treatment around the transition state and provides an overarching description of H^+ transport from the protein via the water molecule toward the buried iron-sulfur cluster. Fig. 6, *A* and *B*, shows typical structures from the umbrella sampling simulation for PT1 and PT2 in state 2. PT1 occurs with the proton-accepting water molecule preferentially arranged near the bulk. During PT2, the same water molecule coordinates to the S1 atom of [3Fe-4S] and the OD1 atom of Asp^{15}. The structural transition from state 2 of PT1 (Fig. 6*A*) to the corresponding state for PT2 (Fig. 6*B*) therefore consists mainly of a rotation of the hydronium ion. The two separate potentials of mean force from Fig. 5, *A* and *C*, describing PT1 and PT2 are shown together in Fig. 6*C*. It should be noted that there is no *a priori* relationship between the two progression coordinates λ_1 and λ_2, which is illustrated by the dashed line that symbolizes the uncharacterized parts of the free energy surface. However, as the two structures of Fig. 6, *A* and *B*, demonstrate, the PES is probably very flat in this region. Because both potentials of mean force do not have a barrier for reaching state 2 (H_3O^+) from their corresponding minima, the merged PMF also consists of only one transition state region with the previously determined forward ($\Delta G^{\ddagger}_{PT1} = 11.7$ kcal/mol) and backward ($\Delta G^{\ddagger}_{PT2} = 23.1$ kcal/mol) barriers.

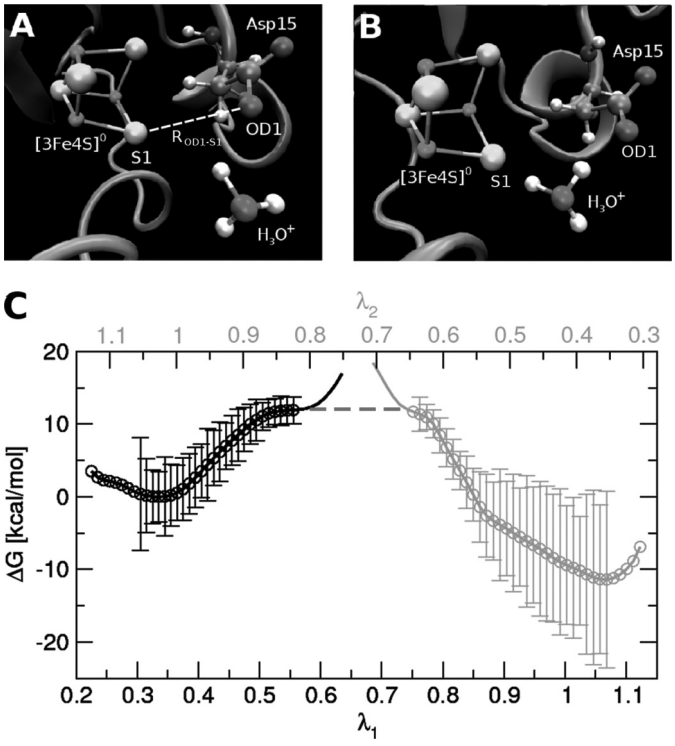

FIGURE 6. *A*, typical structure in state 2 of the PT1 reaction. *B*, same as *A* but for PT2. *C*, combined PMF curves for PT1 (*black*) and PT2 (*gray*) aligned to the same free energy level at $\lambda_1 = 0.56$ and $\lambda_2 = 0.65$ according to the identified H_3O^+ states from the total PT DFT scans evaluated using model A. *Error bars* indicate potential energy fluctuations along λ_1 and λ_2. The postulated transition of the hydronium ion between state 2 of PT1 and PT2 is indicated as a *dashed line*.

In each of the density functional theory scans (models A and B), the initial transfer from OD1 to the water (PT1) is completed at an OD1-HD1 distance of $r_1 = 1.4$ Å and a OD1-OH2 distance of $R_1 = 2.50$ Å. The OH2-HD1 distance at this point therefore is 1.1 Å ($\theta = 180°$), and PT1 is regarded to be completed. Nearly the same average geometry was sampled in the potential of mean force of PT1 using MMPT at $\lambda_1 = 0.56$. This is the region where the surface in Fig. 5*A* is flattening out and suggests completed formation of H_3O^+. Geometries determining state 2 of PT2 were extracted from scans of model A with density functional theory at a S1-OD1 distance of 5.0 Å (*dotted line* in Fig. 3). In this scan, the H_3O^+ species remains stable up to $r_1 = 1.8$ Å. The PT2-related coordinates at this point are $r_2 = 1.96$ Å and $R_2 = 3.00$ Å corresponding to $\lambda_2 = 0.65$, which is the region on the PMF of PT2 (Fig. 5*C*) that exhibits flattening.

DISCUSSION

In the present work, atomistic simulations with provisions to describe hydrogen- or proton-transfer reactions and electronic structure calculations were combined to characterize water-assisted proton transfer in a protein. A concrete procedure for using the MMPT potential in extended and fully solvated condensed-phase systems is presented. The strategy is based on model *ab initio* calculations around critical points of the interaction potential and avoids double counting of nonbonded interactions.

For proton transfer between the Asp^{15} side chain and the buried [3Fe-4S] cluster in FdI, both approaches (MMPT and DFT) support a concerted double PT in which PT1 is the rate-determining step. Previous computational studies also concluded that PT reactions on or near a protein surface proceed semi- to fully concerted rather than stepwise (38, 39, 68). However, these studies were carried out either at the semiempirical level with variational transition state theory (which neglects explicit dynamics) (68) or with calculation of minimum energy pathways on an ensemble of structures (39), or by using density functional theory without dynamics (38).

Computed values for $\Delta G^{\ddagger}_{PT1}$ and $\Delta G^{\ddagger}_{PT2}$ can be directly related to the free energies of activation $\Delta G^{\ddagger}_{on}$ and $\Delta G^{\ddagger}_{off}$ evaluated from experimentally measured rate constants. $\Delta G^{\ddagger}_{PT1}$ (Fig. 5*A*) underestimates $\Delta G^{\ddagger}_{on}$ slightly by 1.6 kcal/mol, whereas $\Delta G^{\ddagger}_{PT2}$ overestimates the experimental barrier $\Delta G^{\ddagger}_{off}$ by 9.0 kcal/mol and is only in qualitative agreement with experiment. Taking zero-point energy corrections into account, both barriers will be further lowered by ≈ 2 kcal/mol. Furthermore, the experimental rate $k^{hop}_{on} = 1294\ s^{-1}$ was measured at a pH of 8.34. At a physiologically more relevant acidic pH (69, 70), the experimental rate for PT2 is smaller ($k^{hop}_{off} = 36 \pm 5\ s^{-1}$ at pH 5.0 (2)), which, according to transition state theory, corresponds to a barrier increase by $\Delta G^{\ddagger}_{PT2} = 1.4$ kcal/mol compared with pH 8.34. In the simulations for PT2, the carboxyl group of Asp^{15} is deprotonated, which covers the situation down to a pH of ≈ 4.1 (the pK_a of Asp lies at 4.1 (71)). Because the measured barriers for proton transfer are pH-dependent, this has to be taken into account in comparing with the computed value. Applying both zero-point corrections (2.0 kcal/mol) and corrections due to the pH dependence (1.4 kcal/mol), the difference between the computed and the experimentally determined barrier for PT2 reduces to 5.6 kcal/mol.

Similarly to this, DFT scans (model compound A) at different R_{OD1-S1} show larger variations of barrier heights for PT2 compared with PT1. A possible effect in umbrella sampling is local relaxation of the environment which can lead to an overstabilization of one state over the other (72). To assess such relaxation effects, 100 individual and unconstrained MMPT MD simulations starting in state 2 ($\lambda_1 = 0.56$ and $\lambda_2 = 0.65$; *i.e.* proton-transferred state) were run and the potential energy along λ_1 and λ_2 was collected until they reached the potential minima. The fluctuations δV of the potential energy (indicated as bars in Fig. 6*C*) remain moderate for PT2 down to $\lambda_2 \approx 0.55$ but increase sharply up to ≈ 10 kcal/mol when approaching geometries of the [3Fe-4S]H$^+$ state. Corresponding fluctuations for PT1 are of similar size for large λ_1 but remain moderate ($\delta V \approx 5$ kcal/mol) for structures around the minimum of PT1. It is important to note that these fluctuations are not "errors;" rather, they reflect the variation in potential energy of downhill dynamics from the TS toward the respective local minimum, and thus, they also exclude entropic contributions. Similar amplitudes for instantaneous relaxation in large condensed phase systems have previously been found to lead to significant changes in barrier heights due to long range forces and global perturbations (73). In conclusion, both DFT and MMPT MD simulations suggest stronger fluctuations for PT2 compared with PT1. An additional reason for the different degrees of agreement of the forward and reverse barriers for PT1 and PT2 is the increased complexity of PT2. PT1 involves

essentially PT between COOH and water, which is a relatively simple process to capture with electronic structure calculations. On the other hand, proton transfer between [3Fe-4S]H^+ and water is much more challenging and quantitative information is likely to be more difficult to obtain.

The transition state energies calculated with models A (smaller, more degrees of freedom relaxed) and B (larger, fewer degrees of freedom relaxed) differ considerably (10.1 kcal/mol *versus* 30.2 kcal/mol). This can be primarily related to the increased flexibility allowed for in model A, which is also supported by the umbrella sampling simulations that find a barrier energy of $\Delta G^{\ddagger}_{on} = 13.3$ kcal/mol. Comparing the structures of model A obtained in the minimum of state 1 with the one of state 3 shows that AcO^- reorients considerably during proton transfer. The RMSD of AcO^- between the two structures aligned to the [3Fe-4S] atoms is 5.8 Å for the scan with $R_{OD1-S1} =$ 5.0 Å. The important structural differences leading to such a large rearrangement are a distance increase of 1 Å between the CG atom of AcOH and the S1 atom of [3Fe-4S] in going from state 1 to state 3 and more noticeably a near inversion of AcOH along the CB-CG vector. This finding corroborates the swinging-arm conduction mechanism suggested from the rapid-scan voltammetry on FdI (2), which is also referred to as a "piggy back" mechanism. Other long range proton-shuttling systems for which the swinging-arm conduction was proposed are NADH or NADPH (74) and bacteriorhodopsin (22). Structures from umbrella sampling simulations in state 1 and state 3 also show an elongation of the CG-S1 distance by ≈ 0.5 Å. On the other hand, a complete inversion of the Asp^{15} side chain along the CB-CG axis in the simulations could not be observed as it is expected to induce major reorientation in the protein backbone. Electronic effects involved in reducing the barrier from 30 kcal/mol to 10 kcal/mol between models A and B can be excluded. For example, Mulliken charges on the atoms involved in PT from structures around the transition state show no significant differences (<0.05 *e*) between models A and B. The DFT profile from model A with $R_{OD1-S1} = 5.0$ Å yields a forward barrier of 10.1 kcal/mol and a reverse barrier of 13.7 kcal/mol, both of which are close to the barriers derived from the experimental rates. All other DFT scans performed in this work (especially those with short R_{OD1-S1}) have their global minimum in state 1. These observations suggest that state 3 in FdI must have larger R_{OD1-S1} compared with the 7FDR x-ray structure. These general conclusions are supported by the umbrella sampling simulations with MMPT, which find $\langle R_{OD1-S1} \rangle = 4.8$ Å in state 1, $\langle R_{OD1-S1} \rangle = 4.5$ Å around the TS, and $\langle R_{OD1-S1} \rangle =$ 5.3 Å after formation of [3Fe-4S]H^+, all consistent with the DFT calculations.

It is worthwhile to mention that relaxed DFT scans for model B at the UB3LYP/6–31G(d,p) level for water-unassisted proton transfer from the −COOH group to the accepting sulfur atom of [3Fe-4S]^0 yield a barrier of $\Delta E \approx 35$ kcal/mol, which makes such a process considerably less likely. Compared with this, water-assisted proton transfer reduces this barrier to $\Delta E \leq 10$ kcal/mol and brings it within the range of experimentally observed rates (2).

In summary, generalized MMPT has been applied to PT in FdI, which involves transport of one proton from the solvent-exposed Asp^{15} residue via a water molecule to a buried [3Fe-4S] cluster. The PMFs from MD simulations show that the hydronium ion (H_3O^+) is not a stable intermediate in the protein cavity. Therefore, the postulated water-mediated PT from Asp^{15} to [3Fe-4S]^0 is most likely a concerted process. Barriers from the present PMF curves qualitatively agree with experimentally determined rate constants of the PT process in FdI. Quantitatively, the forward PMF barrier is in good agreement with experimental data. Our DFT scans using different model systems either over- or underestimated this barrier mainly due to the difficulty of finding a model structure that balances flexibility and protein backbone constraints that affect the conformational dynamics of Asp^{15} (*cf.* swinging-arm mechanism). In addition, the DFT models include only the immediate protein environment without explicit solvent. From such models, no quantitative information can be expected. The present study establishes that it is possible to investigate PT reactions in condensed phase environments, including explicit solvation and at atomistic detail by using generalized MMPT. By studying PT in FdI, MMPT has proven to be a practical tool to simulate multistep PT processes in proteins.

Acknowledgment—Generous allocation of computing time at the CSCS, the Swiss National Supercomputing Centre (Manno, Switzerland) is acknowledged.

REFERENCES

1. Walter, N. G. (2007) *Mol. Cell* **28,** 923–929
2. Hirst, J., Duff, J. L., Jameson, G. N., Kemper, M. A., Burgess, B. K., and Armstrong, F. A. (1998) *J. Am. Chem. Soc.* **120,** 7085–7094
3. Chen, K. S., Hirst, J., Camba, R., Bonagura, C. A., Stout, C. D., Burgess, B. K., and Armstrong, F. A. (2000) *Nature* **405,** 814–817
4. Zhang, L., Wang, L., Kao, Y. T., Qiu, W., Yang, Y., Okobiah, O., and Zhong, D. (2007) *Proc. Natl. Acad. Sci. U.S.A.* **104,** 18461–18466
5. Siwick, B. J., and Bakker, H. J. (2007) *J. Am. Chem. Soc.* **129,** 13412–13420
6. Kadirvelraj, R., Foley, B. L., Dyekjaer, J. D., and Woods, R. J. (2008) *J. Am. Chem. Soc.* **130,** 16933–16942
7. Wlodawer, A., Miller, M., Jaskólski, M., Sathyanarayana, B. K., Baldwin, E., Weber, I. T., Selk, L. M., Clawson, L., Schneider, J., and Kent, S. B. H. (1989) *Science* **245,** 616–621
8. Bolhuis, P. G. (2005) *Biophys. J.* **88,** 50–61
9. Papoian, G. A., Ulander, J., and Wolynes, P. G. (2003) *J. Am. Chem. Soc.* **125,** 9170–9178
10. Fischer, S., and Verma, C. S. (1999) *Proc. Natl. Acad. Sci. U.S.A.* **96,** 9613–9615
11. Gottschalk, M., Dencher, N. A., and Halle, B. (2001) *J. Mol. Biol.* **311,** 605–621
12. Decoursey, T. E. (2003) *Physiol. Rev.* **83,** 475–579
13. Babcock, G. T., and Wikström, M. (1992) *Nature* **356,** 301–309
14. Finbow, M. E., and Harrison, M. A. (1997) *Biochem. J.* **324,** 697–712
15. Parke, C. L., Wojcik, E. J., Kim, S., and Worthylake, D. K. (2010) *J. Biol. Chem.* **285,** 5859–5867
16. Chan, S. I., and Li, P. M. (1990) *Biochemistry* **29,** 1–12
17. Gennis, R. B. (1998) *Proc. Natl. Acad. Sci. U.S.A.* **95,** 12747–12749
18. Belevich, I., Verkhovsky, M. I., and Wikström, M. (2006) *Nature* **440,** 829–832
19. Kim, Y. C., Wikström, M., and Hummer, G. (2009) *Proc. Natl. Acad. Sci. U.S.A.* **106,** 13707–13712
20. Mathies, R. A., Lin, S. W., Ames, J. B., and Pollard, W. T. (1991) *Annu. Rev. Biophys. Biophys. Chem.* **20,** 491–518
21. Du, M., and Fleming, G. R. (1993) *Biophys. Chem.* **48,** 101–111
22. Lanyi, J. K. (1995) *Nature* **375,** 461–463

23. Lanyi, J. K. (1998) *J. Struct. Biol.* **124,** 164–178
24. Garczarek, F., Brown, L. S., Lanyi, J. K., and Gerwert, K. (2005) *Proc. Natl. Acad. Sci. U.S.A.* **102,** 3633–3638
25. Garczarek, F., and Gerwert, K. (2006) *Nature* **439,** 109–112
26. Iwata, T., Paddock, M. L., Okamura, M. Y., and Kandori, H. (2009) *Biochemistry* **48,** 1220–1229
27. Dai, J., Bacic, Z., Huang, X. C., Carter, S., and Bowman, J. M. (2003) *J. Chem. Phys.* **119,** 6571–6580
28. Kaledin, M., Kaledin, A. L., and Bowman, J. M. (2006) *J. Phys. Chem. A* **110,** 2933–2939
29. Wei, D. Q., and Salahub, D. R. (1997) *J. Chem. Phys.* **106,** 6086–6094
30. Sagnella, D. E., and Tuckerman, M. E. (1998) *J. Chem. Phys.* **108,** 2073–2083
31. Pomes, R., and Roux, B. (1996) *J. Phys. Chem.* **100,** 2519–2527
32. Day, T. J., Schmitt, U. W., and Voth, G. A. (2000) *J. Am. Chem. Soc.* **122,** 12027–12028
33. Cheng, H. P. (1996) *J. Phys. Chem.* **105,** 6844–6855
34. Geissler, P. L., Dellago, C., Chandler, D., Hutter, J., and Parrinello, M. (2000) *Chem. Phys. Lett.* **321,** 225–230
35. Meuwly, M., and Karplus, M. (2002) *J. Chem. Phys.* **116,** 2572–2585
36. Mei, H. S., Tuckerman, M. E., Sagnella, D. E., and Klein, M. L. (1998) *J. Phys. Chem. B.* **102,** 10446–10458
37. Liu, Y., and Tuckerman, M. E. (2001) *J. Phys. Chem. B* **105,** 6598–6610
38. Cui, Q., and Karplus, M. (2003) *J. Phys. Chem. B* **107,** 1071–1078
39. Friedman, R., Fischer, S., Nachliel, E., Scheiner, S., and Gutman, M. (2007) *J. Phys. Chem. B* **111,** 6059–6070
40. Warshel, A. (1976) *Nature* **260,** 679–683
41. Bash, P. A., Field, M. J., and Karplus, M. (1987) *J. Am. Chem. Soc.* **109,** 8092–8094
42. Warshel, A., and Weiss, R. M. (1980) *J. Am. Chem. Soc.* **102,** 6218–6226
43. Bala, P., Grochowski, P., Lesyng, B., and McCammon, J. A. (1996) *J. Phys. Chem.* **100,** 2535–2545
44. Lammers, S., and Meuwly, M. (2007) *J. Phys. Chem. A* **111,** 1638–1647
45. Lammers, S., Lutz, S., and Meuwly, M. (2008) *J. Comput. Chem.* **29,** 1048–1063
46. Shen, B., Martin, L. L., Butt, J. N., Armstrong, F. A., Stout, C. D., Jensen, G. M., Stephens, P. J., La Mar, G. N., Gorst, C. M., and Burgess, B. K. (1993) *J. Biol. Chem.* **268,** 25928–25939
47. Meuwly, M., and Karplus, M. (2004) *Biophys. J.* **86,** 1987–2007
48. Bruschi, M., and Guerlesquin, F. (1988) *FEMS Microbiol. Rev.* **54,** 155–175
49. Loerting, T., and Liedl, K. R. (2001) *J. Phys. Chem. A* **105,** 5137–5145
50. Camba, R., Jung, Y. S., Hunsicker-Wang, L. M., Burgess, B. K., Stout, C. D., Hirst, J., and Armstrong, F. A. (2003) *Biochemistry* **42,** 10589–10599
51. Cherepanov, D. A., and Mulkidjanian, A. Y. (2001) *Biochim. Biophys. Acta.* **1505,** 179–184
52. Beratan, D. N., Onuchic, J. N., Winkler, J. R., and Gray, H. B. (1992) *Science* **258,** 1740–1741
53. Page, C. C., Moser, C. C., Chen, X., and Dutton, P. L. (1999) *Nature* **402,** 47–52
54. Meuwly, M., and Karplus, M. (2003) *Faraday Discuss.* **124,** 297–313
55. Ernst, J. A., Clubb, R. T., Zhou, H. X., Gronenborn, A. M., and Clore, G. M. (1995) *Science* **267,** 1813–1817
56. Chandrasekhar, I., Clore, G. M., Szabo, A., Gronenborn, A. M., and Brooks, B. R. (1992) *J. Mol. Biol.* **226,** 239–250
57. Clore, G. M., Bax, A., Wingfield, P. T., and Gronenborn, A. M. (1990) *Biochemistry* **29,** 5671–5676
58. Frisch, M. J., Trucks, G. W., Schlegel, H. B., Scuseria, G. E., Robb, M. A., Cheeseman, J. R., Montgomery, J. A. J., Vreven, T., Kudin, K. N., Burant, J. C., *et al.* (2004) *Gaussian 03*, Revision D.02, Gaussian, Inc., Wallingford, CT
59. Schipke, C. G., Goodin, D. B., McRee, D. E., and Stout, C. D. (1999) *Biochemistry* **38,** 8228–8239
60. Brooks, B. R., Brooks, C. L., 3rd, Mackerell, A. D., Jr., Nilsson, L., Petrella, R. J., Roux, B., Won, Y., Archontis, G., Bartels, C., Boresch, S., Caflisch, A., Caves, L., Cui, Q., Dinner, A. R., Feig, M., Fischer, S., Gao, J., Hodoscek, M., Im, W., Kuczera, K., Lazaridis, T., Ma, J., Ovchinnikov, V., Paci, E., Pastor, R. W., Post, C. B., Pu, J. Z., Schaefer, M., Tidor, B., Venable, R. M., Woodcock, H. L., Wu, X., Yang, W., York, D. M., and Karplus, M. (2009) *J. Comput. Chem.* **30,** 1545–1614
61. MacKerell, A. D., Bashford, D., Bellott, M., Dunbrack, R. L., Evanseck, J. D., Field, M. J., Fischer, S., Gao, J., Guo, H., Ha, S., *et al.* (1998) *J. Phys. Chem. B* **102,** 3586–3616
62. Lammers, S., and Meuwly, M. (2004) *Aust. J. Chem.* **57,** 1223–1228
63. Kottalam, J., and Case, D. A. (1988) *J. Am. Chem. Soc.* **110,** 7690–7697
64. Jorgensen, W. L., Chandrasekhar, J., Madura, J. D., Impey, R. W., and Klein, M. L. (1983) *J. Chem. Phys.* **79,** 926–935
65. Van Gunsteren, W. F., and Berendsen, H. J. (1977) *Mol. Phys.* **34,** 1311–1327
66. Kumar, S., Rosenberg, J. M., Bouzida, D., Swendsen, R. H., and Kollman, P. A. (1995) *J. Comput. Chem.* **16,** 1339–1350
67. Laidler, K. J. (1969) *Theories of Chemical Reaction Rates*, pp. 41–55, McGraw-Hill, New York
68. Smedarchina, Z., Siebrand, W., Fernández-Ramos, A., and Cui, Q. (2003) *J. Am. Chem. Soc.* **125,** 243–251
69. Im, S. C., Liu, G., Luchinat, C., Sykes, A. G., and Bertini, I. (1998) *Eur. J. Biochem.* **258,** 465–477
70. Sétif, P., Fischer, N., Lagoutte, B., Bottin, H., and Rochaix, J. D. (2002) *Biochim. Biophys. Acta* **1555,** 204–209
71. Berg, J. M., Tymoczko, J. L., and Stryer, L. (2002) *Biochemistry*, 5th Ed., p. 96, W. H. Freeman, New York
72. Banushkina, P., and Meuwly, M. (2005) *J. Phys. Chem. B* **109,** 16911–16917
73. Zheng, C., Makarov, V., and Wolynes, P. G. (1996) *J. Am. Chem. Soc.* **118,** 2818–2824
74. Williams, R. J. (1988) *Annu. Rev. Biophys. Biol.* **17,** 71–97

Supplemental Data: Water-assisted Proton Transfer in Ferredoxin I

Stephan Lutz, Ivan Tubert-Brohman, Yonggang Yang, Markus Meuwly

MMPT FORCE FIELD DESCRIPTION

In the initial MMPT studies (1, 2) V_{PT} was fitted to ab initio data for model systems including $H_2O\cdots H^+\cdots OH_2$ (prototype for a symmetric single minimum), $H_3N\cdots H^+\cdots NH_3$ (symmetric double minimum), and $H_3N\cdots H^+\cdots OH_2$ (asymmetric double minimum). The functional form of the latter which was also used in the present work to describe PT1 and PT2 is of the following form:

$$\begin{aligned} V_{\mathrm{PT}}(R,\rho,\theta) &= D_{eq,1}(R)\left[1-\exp(-\beta_1(R)(\rho-\rho_{eq,1}(R)))\right]^2 \\ &+ D_{eq,2}(R)\left[1-\exp(-\beta_2(R)(\rho_{eq,2}(R)-\rho))\right]^2 \\ &- c(R)+k\theta^2 \end{aligned} \tag{1}$$

where the parameters $D_{eq,i}$, β_i, $\rho_{eq,i}$, and c are functions of R, and k is a constant:

$$D_{eq,1}(R) = p_1\left(1-\exp(-p_2(R-p_3)\right)^2+p_4 \tag{2}$$

$$\beta_1(R) = \frac{p_5}{1-\exp(-p_6(R-p_7))} \tag{3}$$

$$\rho_{eq,1}(R) = p_8(1-\exp(-p_9(R-p_{10}))^2+p_{11} \tag{4}$$

$$D_{eq,2}(R) = p_{12}(1-\exp(-p_{13}(R-p_{14}))^2+p_{15} \tag{5}$$

$$\beta_2(R) = \frac{p_{16}}{1-\exp(-p_{17}(R-p_{18}))} \tag{6}$$

$$\rho_{eq,2}(R) = p_{19}(1-\exp(-p_{20}(R-p_{21}))^2+p_{22} \tag{7}$$

$$c(R) = p_{23}(1-\exp(-p_{24}(R-p_{25}))^2+p_{26} \tag{8}$$

$$k = p_{27} \tag{9}$$

The specific chemical environment can be taken into account by morphing the entire PES through coordinate transformations (3, 4). Here, the previously morphed asymmetric PES parameters p_{i} for the proton transfer between acetic acid and water was used for PT1 (2) which are listed in Table S1.

	$D_1(R)$		$\beta_1(R)$		$R_{eq,1}(R)$
p_1	24.636 kcal/mol	p_5	3.849	p_8	-0.076
p_2	1.668 Å^{-1}	p_6	2.149 Å^{-1}	p_9	1.894 Å^{-1}
p_3	3.030 Å	p_7	2.594 Å	p_{10}	2.458 Å
p_4	161.889 kcal/mol			p_{11}	0.155
	$D_2(R)$		$\beta_2(R)$		$R_{eq,2}(R)$
p_{12}	25.553 kcal/mol	p_{16}	4.988	p_{19}	0.063
p_{13}	1.342 Å^{-1}	p_{17}	2.252 Å^{-1}	p_{20}	1.770 Å^{-1}
p_{14}	3.031 Å	p_{18}	2.521 Å	p_{21}	2.650 Å
p_{15}	69.245 kcal/mol			p_{22}	0.848
	c		k		
p_{23}	36.007 kcal/mol	p_{27}	0.009 kcal/mol/deg		
p_{24}	0.863 Å^{-1}				
p_{25}	2.746 Å				
p_{26}	58.910 kcal/mol				

Table S1: The parameter set for the fit of the proton transfer potential from AcOH to a water (2).

PT2 takes place between H_3O^+ and the S1 sulfur atom of a [3Fe-4S] cluster. Nonbonded interactions of the atoms involved in the proton transfer with the remaining [3Fe-4S] cluster atoms play a potentially important role as this model system is larger compared to the model system used to fit PT1. Therefore, the asymmetric double minimum PES for $H_3N\cdots H^+\cdots OH_2$ (2) was used as a zeroth order model to refit all parameters p_i, describing the R and ρ dependence to the electronic structure calculations removing double counted nonbonding interactions. The purely DFT calculated PES of PT2 is shown in Fig. S1A. V_{PT} was fitted to the difference between the DFT energy $V(\vec{x})$ and the energy computed using the CHARMM force field when V_{PT} is set to zero:

$$V_{PT}(R_2,\rho_2,\theta_2) = V(\vec{x}) - V_{MM}(\vec{y}). \tag{10}$$

This relation is shown graphically in Fig. S1B. Fig. S1C reports the potential $V(\vec{x}) - V_{MM}(\vec{y})$ over the complete range of ab initio calculated geometries from model C and its least-squares fitted potential $V_{PT2}(R_2,\rho_2,\theta_2)$ is shown in Fig. S1D. The fit reproduces all essential features of the DFT PES in Fig. S1A. The mean absolute deviation over the entire surface is 2.4 kcal/mol, with the large deviations concentrated around the high energy regions which are of limited chemical interest. If one considers only the region below 10 kcal/mol above the minimum, the mean absolute deviation is only 0.9 kcal/mol. The most noticeable difference between the two PESs is the location of their absolute minima which shifts from

$R_2 = 3.5$ in the DFT PES (Fig. S1A) to $R_2 = 3.9$ Å in the MMPT PES (Fig. S1D). The energy difference of these two configurations in the DFT surface is only 0.4 kcal/mol meaning there is a very flat valley connecting the two coordinates.

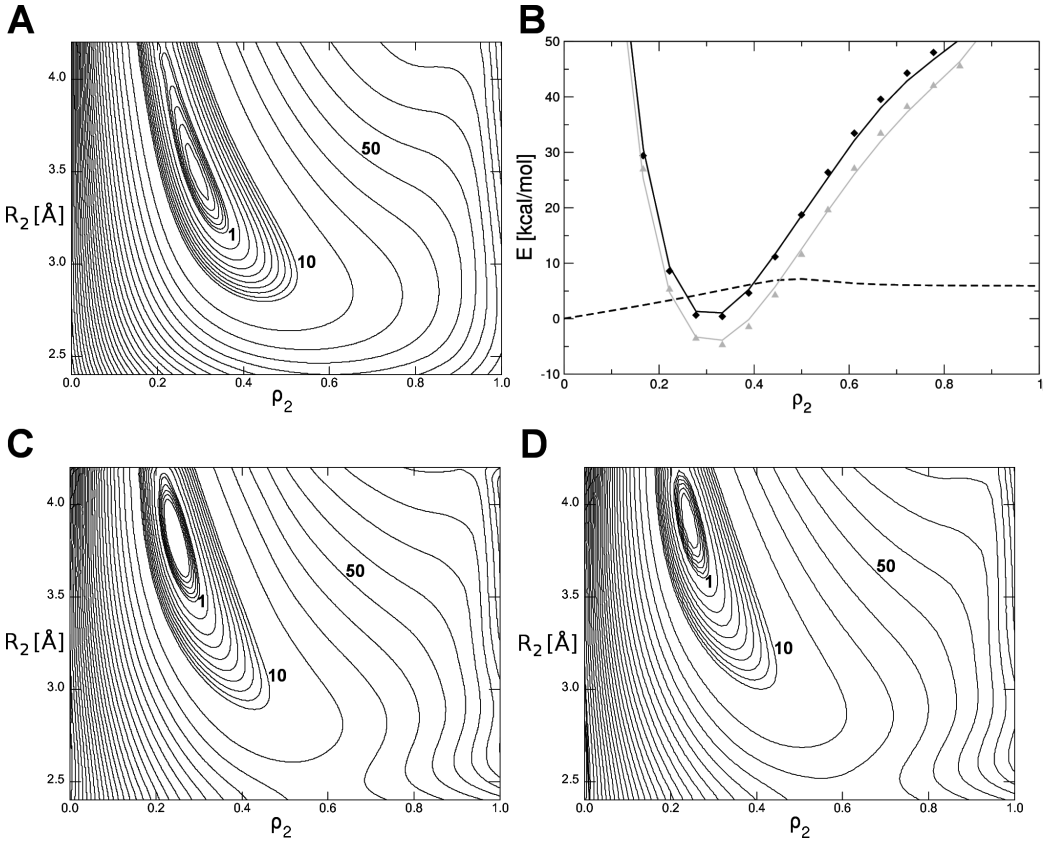

Fig. S1: A: Contour plot of the potential energy surface resulting from the DFT scan on model C along $\rho_2 = (r_2 - 0.8)/(R_2 - 1.6)$ and R_2. B: Example of the fitting process to used to avoid double counting of the molecular mechanics non-bonded terms. V_{PT} is fitted to the difference between the DFT energy and V_{MM}. The slice shown is for constant $R_2 = 3.36$ Å. Black diamonds: $V^{ref}(\vec{x})$, which is the DFT energy; dotted black line: $V_{MM}(\vec{y})$, which is the MM energy calculated when V_{PT} is set to zero; grey triangles: $V^{ref}(\vec{x}) - V_{MM}(\vec{y})$; grey line: $V_{PT}(R_2, \rho_2, \theta_2)$, obtained from a least-squares fit of eq. 1 to the grey triangles; black line: total fitted MMPT potential $V^{fit}(\vec{x})$. C: Contour plot of the reference potential to be fitted, $V^{ref}(\vec{x}) - V_{MM}(\vec{y})$. D: Contour plot of $V_{PT2}(R_2, \rho_2, \theta_2)$, obtained as a least-squares fit of eq. 1 to the potential in C which was used in the MD simulations. Contour lines are plotted between 0.0 kcal/mol and 1.0 kcal/mol in steps of 0.2 kcal/mol, between 1 and 10 kcal/mol in steps of 1.0 kcal/mol and above 10 kcal/mol in steps of 10.0 kcal/mol.

Parameters p_i fitted to the corrected PES in Fig. S1D for the proton transfer from [3Fe-4S]$H^+$to water are listed in Table S2. k is not part of the fit and was set to 0.011 kcal/mol/deg^2 which is an empirically robust value as found from the previously fitted MMPT systems (2).

$D_1(R)$		$\beta_1(R)$		$R_{eq,1}(R)$	
p_1	36.095 kcal/mol	p_5	5.868	p_8	-0.984
p_2	-0.072 Å^{-1}	p_6	1.227 Å^{-1}	p_9	1.516 Å^{-1}
p_3	-10.852 Å	p_7	3.131 Å	p_{10}	1.619 Å
p_4	-39.565 kcal/mol			p_{11}	1.166
$D_2(R)$		$\beta_2(R)$		$R_{eq,2}(R)$	
p_{12}	127.153 kcal/mol	p_{16}	15.133	p_{19}	1.266
p_{13}	-0.166 Å^{-1}	p_{17}	2.646 Å^{-1}	p_{20}	2.823 Å^{-1}
p_{14}	2.883 Å	p_{18}	3.275 Å	p_{21}	2.389 Å
p_{15}	0.362 kcal/mol			p_{22}	-0.333
c		k			
p_{23}	-349.642 kcal/mol	p_{27}	0.011 kcal/mol/deg		
p_{24}	-0.187 Å^{-1}				
p_{25}	4.337 Å				
p_{26}	74.532 kcal/mol				

Table S2: The set of asymmetric MMPT parameters obtained from the fit to the B3LYP/6-31G(d,p) scan.

PROTON TRANSFER REACTION COORDINATE CONVERSION

For practical reasons the free energy of activation $\Delta G^{\ddagger}$ was computed along the coordinate $\lambda = r/R$. Fig. S2 shows how λ is related to R and ρ.

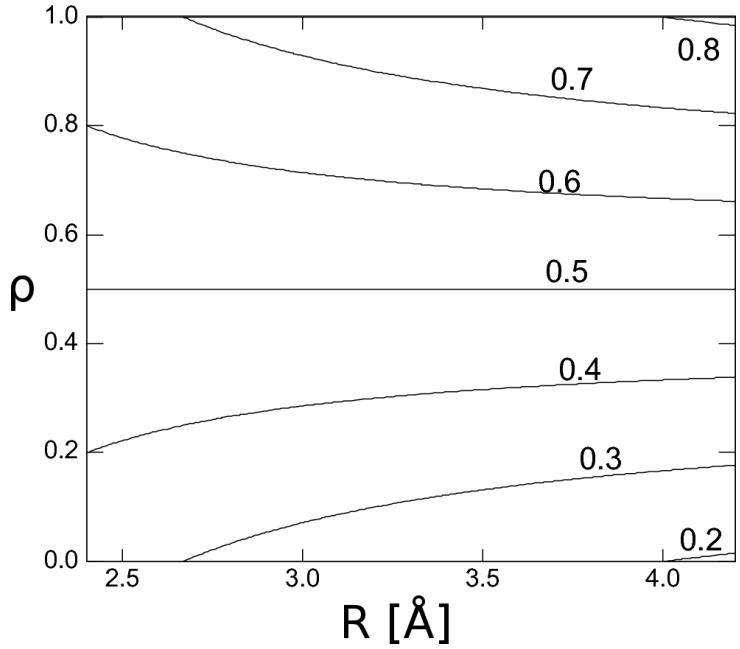

Fig. S2: Reaction coordinate reduction; contour plot of $\lambda = r/R$ as a function of R and ρ.

FLUCTUATING CHARGE DESCRIPTION

In the former MMPT study (2), PT1 from Asp15 to a water molecule was considered and the standard CHARMM charges on the donor, the transfered hydrogen, and the OH2 acceptor atoms were kept fixed. However, this is only approximately true and it can be expected that charge transfer accompanies proton transfer which accounts for the difference of the free energy barrier of 3.5 kcal/mol for PT1 between the former and the present simulation. Therefore, in the present work, the charges on the atoms involved in proton transfers were gradually scaled along the reaction coordinate for both reactions, PT1 and PT2. The charges on each atom were evaluated from the Mulliken charges extracted from the asymmetric DFT potential energy surfaces computed for PT1 (2) and PT2 (Figure 2A) at $\rho = 0.0$, $\rho = 0.5$, $\rho = 1.0$, and $R = 2.4$ Å with the Gaussian03 suite of programs (5) and are listed in Table S3.

Atom	**Charge (e)**				
	Used for fit	NBO	Mull. $\rho_2 = 0$	Mull. $\rho_2 = 0.5$	Mull. $\rho_2 = 1$
3 Fe	0.68	1.25	0.48	0.47	0.47
3 S2 to S4	-0.30	-0.92 (-1.0)	-0.58	-0.59	-0.62
1 S1	-0.30	-0.92	-0.59	-0.76	-0.95
1 H2	0.13		0.17	0.30	0.27
1 O	-0.834		-0.57	-0.49	-0.19
2 H (water)	0.417		0.30	0.31	0.33
3 S (MeS)	-0.70		-0.34	-0.34	-0.35
3 C	-0.50		-0.45	-0.44	-0.44
9 H	0.07		0.11	0.11	0.11

Table S3: Charges used for the fitting. The NBO charges used in the previous paper are included for comparison, as well as the Mulliken charges from three points along the PES in Fig. S1A ($R_2 = 2.4$ for all three points).

The charges together with a fitted quadratic function along each ρ of every atom is shown in Fig. S2. From $\rho_1 = 0$ to $\rho_1 = 1$ for PT1 the charge on the OD1 donor atom decreases nearly linearly from -0.46 to -0.57 e. On the hydrogen HD1 it rises first from 0.28 to 0.36 e at $\rho_1 = 0.5$ and decreases to 0.26 e at $\rho_1 = 1$. Most of the positive charge is transferred to OH2 which initially carries -0.59 e and ends up having -0.25 e of charge after PT1 has completed. Similarly, for PT2 the charge on S1 decreases from $\rho_2 = 0$ to $\rho_2 = 1$ from -0.60 to -0.95 e. On HS it rises from 0.17 to 0.30 e at $\rho_2 = 0.5$ and decreases again to 0.27 e at $\rho_2 = 1$. Like for PT1 the charge on OH2 which initially carries -0.58 e rises to -0.20 e after the completed PT2. For each umbrella sampling window the charges on donor, hydrogen, and acceptor atoms were set to the corresponding value obtained by the fit in Fig. S3 at the related equilibrium distance of the biasing potential.

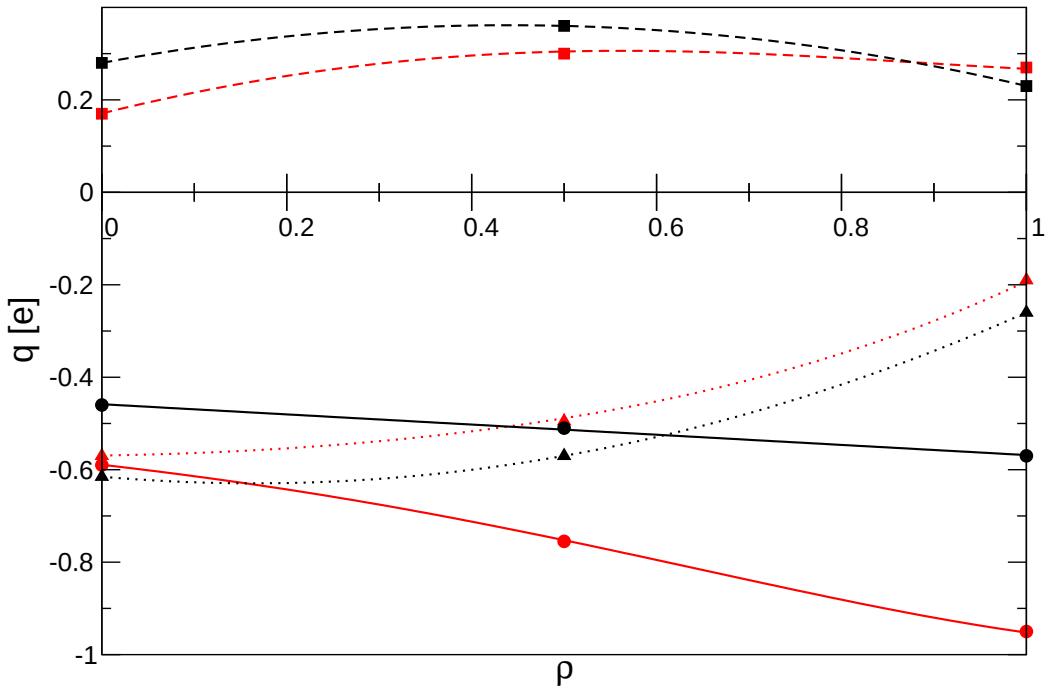

Fig. S3: Charge transfer along ρ_1 (black) and ρ_2 (red) for donor (circles, solid lines), hydrogen (squares, dashed lines), and acceptor atoms (triangles, dotted lines). Symbols: Mulliken charges computed at $R = 2.4$ Å of the corresponding asymmetric DFT potentials used for fitting the MMPT parameters of PT1 and PT2. Lines: Functional fit through the individual charges plotted at $\rho = 0.0$, $\rho = 0.5$, and $\rho = 1.0$.

FULL CITATIONS

Missing authors in the list of references from the main article for Gaussian (5) and CHARMM (6, 7) are added in the following.

References

[1] Lammers, S., and Meuwly, M. (2004) *Aust. J. Chem.* **57**, 1223 – 1228.

[2] Lammers, S., Lutz, S., and Meuwly, M. (2008) *J. Comp. Chem.* **29**, 1048 – 1063.

[3] Meuwly, M., and Hutson, J. M. (1999) *J. Chem. Phys.* **110**, 8338 – 8347.

[4] Lammers, S., and Meuwly, M. (2007) *J. Phys. Chem. A* **111**, 1638 – 1647.

[5] Frisch, M. J., Trucks, G. W., Schlegel, H. B., Scuseria, G. E., Robb, M. A., Cheeseman, J. R., Montgomery, J. A. J., Vreven, T., Kudin, K. N., Burant, J. C., Millam, J. M., Iyengar, S. S., Tomasi, J., Barone, V., Mennucci, B., Cossi, M., Scalmani, G., Rega, N., Petersson, G. A., Nakatsuji, H., Hada, M., Ehara, M., Toyota, K., Fukuda, R., Hasegawa, J., Ishida, M., Nakajima, T., Honda, Y., Kitao, O., Nakai, H., Klene, M., Li, X., Knox, J. E., Hratchian, H. P., Cross, J. B., Adamo, C., Jaramillo, J., Gomperts, R., Stratmann, R. E., Yazyev, O., Austin, A. J., Cammi, R., Pomelli, C., Ochterski, J. W., Ayala, P. Y., Morokuma, K., Voth, G. A., Salvador, P., Dannenberg, J. J., Zakrzewski, V. G., Dapprich, S., Daniels, A. D., Strain, M. C., Farkas, O., Malick, D. K., Rabuck, A. D., Raghavachari, K., Foresman, J. B., Ortiz, J. V., Cui, Q., Baboul, A. G., Clifford, S., Cioslowski, J., Stefanov, B. B., Liu, G., Liashenko, A., Piskorz, P., Komaromi, I., Martin, R. L., Fox, D. J., Keith, T., Al-Laham, M. A., Peng, C. Y., A., , Nanayakkara, M., Challacombe, P. M. W., Gill, Johnson, B., Chen, W., Wong, M. W., Gonzalez, C., and Pople, J. A. (2004) Gaussian 03, Revision D.02. Gaussian, Inc., Wallingford CT, U.S.A.

[6] MacKerell, A. D., Bashford, D., Bellott, M., Dunbrack, R. L., Evanseck, J. D., Field, M. J., Fischer, S., Gao, J., Guo, H., Ha, S., Joseph-Mccarthy, D., Kuchnir, L., Kuczera, K., Lau, F. T. K., Mattos, C., Michnick, S., Ngo, T., Nguyen, D. T., Prodhom, B., Reiher, W. E., Roux, B., Schlenkrich, M., Smith, J. C., Stote, R., Straub, J., Watanabe, M., Wiorkiewicz-Kuczera, J., Yin, D., and Karplus, M. (1998) *J. Phys. Chem. B* **102**, 3586 – 3616.

[7] Brooks, B. R., Brooks, C. L., Mackerell, A. D., Nilsson, L., Petrella, R. J., Roux, B., Won, Y., Archontis, G., Bartels, C., Boresch, S., Caflisch, A., Caves, L., Cui, Q., Dinner, A. R., Feig, M., Fischer, S., Gao, J., Hodoscek, M., Im, W., Kuczera, K., Lazaridis, T., Ma, J., Ovchinnikov, V., Paci, E., Pastor, R. W., Post, C. B., Pu, J. Z., Schaefer, M., Tidor, B., Venable, R. M., Woodcock, H. L., Wu, X., Yang, W., York, D. M., and Karplus, M. (2009) *J. Comp. Chem.* **30**, 1545 – 1614.

Water-assisted Proton Transfer in Ferredoxin I

Stephan Lutz, Ivan Tubert-Brohman, Yonggang Yang and Markus Meuwly

J. Biol. Chem. 2011, 286:23679-23687.
doi: 10.1074/jbc.M111.230003 originally published online April 29, 2011
